



ALMA MATER STUDIORUM  
UNIVERSITÀ DI BOLOGNA

ARCHIVIO ISTITUZIONALE  
DELLA RICERCA

## Alma Mater Studiorum Università di Bologna Archivio istituzionale della ricerca

Effect of extended surfaces on lauric acid melting process in annular cavities

This is the final peer-reviewed author's accepted manuscript (postprint) of the following publication:

*Published Version:*

Spengler, F.C., Oliveski, R.D.C., Rocha, L.A.O., Biserni, C. (2022). Effect of extended surfaces on lauric acid melting process in annular cavities. JOURNAL OF ENERGY STORAGE, 46, 1-11 [10.1016/j.est.2021.103867].

*Availability:*

This version is available at: <https://hdl.handle.net/11585/880001> since: 2022-03-28

*Published:*

DOI: <http://doi.org/10.1016/j.est.2021.103867>

*Terms of use:*

Some rights reserved. The terms and conditions for the reuse of this version of the manuscript are specified in the publishing policy. For all terms of use and more information see the publisher's website.

This item was downloaded from IRIS Università di Bologna (<https://cris.unibo.it/>).  
When citing, please refer to the published version.

(Article begins on next page)

This is the final peer-reviewed accepted manuscript of:

Fernando Claudio Spengler, Rejane De Césaró Oliveski, Luiz Alberto Oliveira Rocha, Cesare Biserni

Effect of extended surfaces on lauric acid melting process in annular cavities

In *Journal of Energy Storage*, Volume 46, 2022

The final published version is available online at:

<https://doi.org/10.1016/j.est.2021.103867>

Rights / License:

The terms and conditions for the reuse of this version of the manuscript are specified in the publishing policy. For all terms of use and more information see the publisher's website.

This item was downloaded from IRIS Università di Bologna (<https://cris.unibo.it/>)

**When citing, please refer to the published version.**

## NUMERICAL INVESTIGATION ON LURIC ACID MELTING PROCESS IN HEAT EXCHANGERS: EFFECT OF THE FIN GEOMETRIC PARAMETERS

Fernando Claudio Spengler<sup>1</sup>, Rejane De Césaró Oliveski<sup>1</sup>, Luiz Alberto Oliveira Rocha<sup>1</sup>, and Cesare Biserni<sup>2</sup>

<sup>1</sup>Mechanical Engineering Graduate Program, Universidade do Vale do Rio dos Sinos, 93022-750 São Leopoldo, Brazil

<sup>2</sup>Department of Industrial Engineering, Alma Mater Studiorum, University of Bologna, Viale Risorgimento 2, 40136 Bologna, Italy.

1 **Abstract.** *Thermal energy storage makes it possible to adjust energy availability and*  
2 *demand. Systems that use latent heat storage (LHTES) have high energy density and*  
3 *low thermal variation during the charge and discharge cycles. The phase change*  
4 *materials (PCM) used in these systems generally have low thermal conductivity, which*  
5 *makes the energy charge and discharge cycles prolonged. To enhance the heat*  
6 *exchange in these systems, several approaches have been presented in the literature.*  
7 *Among these different solutions, the use of extended surfaces has shown good results.*  
8 *The effect related to the variation of the fins geometric proportions on the PCM melting*  
9 *process is still a gap, and the present work aims to analyze the effect of the fins*  
10 *positioning and aspect ratio variation, in an annular cavity, filled with lauric acid. In*  
11 *total, 46 geometric configurations of the fin were studied, keeping constant its*  
12 *transversal area (length x thickness), but varying between 5 aspect ratios (length /*  
13 *thickness), for 5 different area ratios (fin area / cavity area). The study was performed*  
14 *by numerical simulation with the finite volume method. The numerical model is*  
15 *composed of the continuity, momentum conservation, and energy conservation*  
16 *equations, plus the enthalpy-porosity phase change model. It was validated with the*  
17 *experimental results of the literature. The computational mesh was evaluated using*  
18 *the Grid Convergence Index (GCI), resulting in an average index of 0.003%. For the*  
19 *analysis of the results, the melting time was considered as a performance indicator.*  
20 *The different heat exchange behaviors throughout the phase change process are*  
21 *analyzed in terms of liquid fraction vs Fourier and Nusselt number vs. Fourier. The*  
22 *melting enhancement of the studied cases is also analyzed. This set of results showed*  
23 *that: the total melting time in systems with vertical fin arrangements is approximately*  
24 *44% less than in systems with horizontal fin arrangements; the melting rate in systems*  
25 *with horizontal fin arrangements is 15% higher than systems with vertical fins, while*

26 *there is solid PCM in the upper region of the cavity; for systems with area ratio*  
 27  *$\phi = 0.003$ , the increase in the fin aspect ratio entails in a total melting time reduction*  
 28 *higher than 11% in vertical fins arrangements, and lower than 2% in horizontal fins*  
 29 *arrangements.*

30 **Keywords:** *CFD. PCM. Lauric Acid. Melting. Fins.*

### 31 **Nomenclature**

32	$A$	area	$[m^2]$
33	$a$	fin width	$[m]$
34	$b$	fin length	$[m]$
35	$C$	mushy zone constant	$[kg\ m^{-3}\ s^{-1}]$
36	$c_p$	specific heat	$[J\ kg^{-1}\ K^{-1}]$
37	$D$	diameter	$[m]$
38	$dt$	time step	$[s]$
39	$e$	error	$[-]$
40	$Fo$	Fourier number	$[-]$
41	$g$	gravity acceleration	$[m\ s^{-2}]$
42	$GCI$	grid convergence index	$[-]$
43	$h$	heat transfer coefficient	$[W\ m^{-2}\ K^{-1}]$
44	$hr$	representative mesh size	$[-]$
45	$k$	thermal conductivity	$[W\ m^{-1}\ K^{-1}]$
46	$L$	latent heat	$[J\ kg^{-1}]$
47	$L_c$	characteristic length	$[m]$
48	$m$	mass	$[kg]$
49	$N$	number of elements	$[-]$
50	$Nu$	Nusselt number	$[-]$
51	$p$	pressure	$[Pa]$
52	$\dot{Q}$	heat transfer rate	$[W]$
53	$q''$	heat flow	$[W\ m^{-2}]$
54	$R$	radius	$[m]$
55	$AR$	aspect ratio	$[-]$
56	$\vec{S}$	source term	$[Pa\ m^{-1};\ W\ m^{-3}]$
57	$T$	temperature	$[K]$

58	$t$	time	[s]
59	$\vec{V}$	velocity vector	[m s <sup>-1</sup> ]
60	<b><i>Greek Symbols</i></b>		
61	$\alpha$	thermal diffusivity	[m <sup>2</sup> s <sup>-1</sup> ]
62	$\beta$	liquid fraction	[-]
63	$\gamma$	volume fraction	[-]
64	$\Delta$	variation	[-]
65	$\varepsilon$	numeric constant	[-]
66	$\zeta$	thermal expansion coefficient	[K <sup>-1</sup> ]
67	$\eta_f$	fin efficiency	[-]
68	$\lambda$	specific enthalpy	[J kg <sup>-1</sup> ]
69	$\mu$	dynamic viscosity	[kg m <sup>-1</sup> s <sup>-1</sup> ]
70	$\nu$	kinematic viscosity	[m <sup>2</sup> s <sup>-1</sup> ]
71	$\rho$	density	[kg m <sup>-3</sup> ]
72	$\phi$	fraction of fin area in cavity	[-]
73	<b><i>Subscripts</i></b>		
74	$0$	without fins	
75	$cr$	<i>critical</i>	
76	$ext$	external	
77	$f$	fin	
78	$i$	element	
79	$int$	internal	
80	$l$	liquid	
81	$m$	melting	
82	$min$	minimum	
83	$s$	solid	
84	$se$	section	
85	$w$	wall	

## 1 Introduction

86 Phase change materials (PCM) systems for heating and cooling solutions are  
87 used in a variety of areas such as building construction; vehicle thermal comfort;  
88 medical, pharmaceutical and chemical transport solutions; electronic cooling; solar  
89 water heating systems, the textile industry [1]. These latent heat storage systems  
90 (LHTES) have high energy storage density resulting in a more compact energy storage  
91 system [2]. Moreover, they benefit from constant temperature (for pure substances)  
92 during energy charge and discharge [3].

93 Thermal comfort solutions normally require a temperature range between 0 and  
94 60 °C. This temperature range is compatible with the phase change (solid-liquid) of  
95 organic PCM. Which are and widely available in nature, besides being non-toxic, non-  
96 corrosive, and chemically stable. However, most PCM has low thermal conductivity.  
97 This fact eventually requires techniques for increasing heat transfer to optimize energy  
98 loading and unloading rates [2]. Several methods have been proposed in literature  
99 such as: bubble agitation [4]; micro-encapsulation [5]; metal-matrix insertion [6]; high-  
100 conductivity particle dispersion [7]; nano-particle addition [8]; PCM mixture [9] and  
101 metal foam immersion [10]. Among these methods, the application of extended  
102 surfaces presents good results for improving the PCM melting rate [1].

103 Annular arrangements are widely used in thermal systems due to less heat loss  
104 than other configurations [11]. Thereby, annular section geometries represent more  
105 than 70% of LHTES publications. The ratio between the hull and the tube's diameter  
106 is linked to the energy storage capacity and the phase change rate of the material. In  
107 this configuration, longitudinal, radial, or pin-shaped fins can be used. Among these,  
108 the longitudinal fins are the most widespread, probably due to the ease of design and  
109 manufacture while providing high heat exchange efficiency [12].

110 Several studies have already been conducted on the effect of the geometry of  
111 annular section LHTES. Darzi, Farhadi, and Sedighi [13] and Pahamli et al. [14-15], for  
112 example, investigated the effect of the eccentricity of tubes in annular sets. Al-Abidi et  
113 al. [16], Mat et al. [17], and Rathod and Banerjee [18] found improvement in the  
114 efficiency of LHTES with multiple longitudinal fins. New fin geometries have been  
115 proposed by Abdulateef et al. [19] and Sciacovelli, Gagliardi, and Verda [20]. Variations  
116 in the geometry of the tube itself were tested by Darzi, Jourabian, and Farhadi [21].  
117 Wang et al. [22] and Yuan et al. [23] presented the effect of the fins tilt angle. Mahdi

118 and Nsofor [24-25] studied the use of fins in a system with nanoparticles. The effect of  
 119 the length of the fins was addressed by Ji et al. [26]. Optimization studies and  
 120 innovative longitudinal fin configurations were presented by Deng et al. [27] and Mahdi  
 121 et al [28-29].

122 Finned cylindrical cavities filled with PCM have already proven to be effective  
 123 and meet practical needs. Although there are different proposals for improvement, the  
 124 fins proportions variation effect, in the PCM melting process, has not yet been explored  
 125 in other studies. Thus, this work aims to analyze the effect of the fins proportions and  
 126 arrangements on the lauric acid melting process, inside an annular cavity, using bi-  
 127 dimensional computational fluid dynamics.

## 128 2 Problem Presentation

129 The studied heat exchanger has an annular section with internal radius  
 130 ( $R_{int} = 20$  mm) and external radius ( $R_{ext} = 40$  mm). The fins have a length ( $l_f$ ) and  
 131 thickness ( $e_f$ ). The annular cavity is filled with lauric acid, initially in the solid-state. As  
 132 shown in Figs. 1(a-b), were studied two fins arrangements: horizontal and vertical,  
 133 respectively.

134 Total melting time ( $t_m$ ) is the usual performance indicator for latent energy  
 135 systems. As shown in the flowchart of Fig. 2, the dimensional definition of the fins intent  
 136 to evaluate the design concerning the best efficiency of the system.

137 The transversal areas of the fins ( $A_f$ ) and cavity ( $A_{se}$ ) are obtained by Eq. (1)  
 138 and (2), respectively, considering the heat exchanger with the annular section shown  
 139 in Fig. 1. The cavity area is constant in all cases. The area of the fins varies according  
 140 to the different proportions of occupation ( $\phi$ ) obtained by Eq. (3). The degrees of  
 141 freedom and parameters of the system are defined by the aspect ratio ( $AR$ ), according  
 142 to Eq. (4), where  $\Delta R = R_{ext} - R_{int}$ :

$$143 \quad A_f = H_f e_f \quad (1)$$

$$144 \quad A_{se} = \pi(R_{ext}^2 - R_{int}^2) \quad (2)$$

$$146 \quad \phi = \frac{A_f}{A_{se}} \quad (3)$$

147

148

$$AR = \frac{l_f}{\Delta R}. \quad (4)$$

149

150

151

152

153

154

155

156

Initially, 5 different values of  $\phi$  were defined: 0.003, 0.005, 0.01, 0.02 and 0.03. Also, 5 values of  $AR$  were defined: 1/8, 1/4, 1/2, 3/4, and 7/8. Since  $A_{se}$  is constant, 5 different values of  $A_f$  were obtained from Eq. (3). For each value of  $\phi$ , 5 vertical fins and 5 horizontal fins were studied, and the values of  $l_f$  were obtained from eq. (4). Thus,  $e_f$  was obtained as  $e_f = A_f / L_f$ . All the dimensions analyzed are shown in Tab. 1. However,  $e_f$  value for  $AR = 1/8$  and  $\phi = 0.02$  and  $0.03$  is not physically viable, as it exceeds the value of  $\Delta R$ .

157

158

159

160

161

162

The lauric acid is a saturated fatty acid used on an industrial scale. It is characterized by biodegradability, chemical stability, non-toxicity, high availability, and low cost. Besides, it presents a small volumetric variation during phase change [30-31]. Table 2 present the thermophysical properties of lauric acid, with the values of specific heat ( $c_p$ ), latent heat ( $L$ ), melting temperature ( $T_m$ ), thermal conductivity ( $k$ ), thermal expansion coefficient ( $\zeta$ ), density ( $\rho$ ), and dynamic viscosity ( $\mu$ ).

163

## 2.1 Mathematical Model

164

165

166

167

The mathematical model is composed of the equations of continuity (5), momentum (6), and energy conservation (7) plus the *enthalpy-porosity* phase change model (8-12) of Voller e Prakash [32].

168

$$\frac{\partial \rho}{\partial t} + \nabla(\rho \vec{V}) = 0 \quad (5)$$

169

170

$$\frac{\partial \rho \vec{V}}{\partial t} + \nabla(\rho \vec{V} \vec{V}) = -\nabla p + \nabla(\mu \nabla \vec{V}) + \rho \vec{g} + \vec{S} \quad (6)$$

171

172

$$\frac{\partial(\rho \lambda)}{\partial t} + \nabla(\rho \vec{V} \lambda) = \nabla(k \nabla T), \quad (7)$$

173

174 Where  $t$  is the time,  $p$  is the pressure,  $\vec{g}$  is the acceleration of gravity,  $\lambda$  is the total  
 175 enthalpy,  $\vec{V}$  is the velocity vector,  $\rho$  is the density, and  $\vec{S}$  is the source term given by  
 176 Eq. (8)

$$177 \quad \vec{S} = \frac{(1-\gamma)^2}{(\gamma^3 + \varepsilon)} C \vec{V}. \quad (8)$$

178 In Eq. (8),  $\varepsilon = 0.001$  is a constant, to avoid division by zero,  $C$  is the constant of the  
 179 porous zone, related to its morphology [32],  $\gamma$  is the volume fraction of solid and liquid,  
 180 obtained through Eq. (9),

$$181 \quad \gamma = \begin{cases} 0 & \text{se } T < T_s \\ 1 & \text{se } T > T_l \\ \frac{T-T_s}{T_l-T_s} & \text{se } T_s < T < T_l \end{cases} \quad (9)$$

where  $T_s$  is the temperature of the solid and  $T_l$  the temperature of the liquid.

The total enthalpy ( $\lambda$ ) is obtained by adding the sensitive enthalpy ( $\lambda_{sen}$ ) and the variation of the enthalpy in the phase change ( $\lambda_L$ ). The sensitive enthalpy ( $\lambda_{sen}$ ) is given by Eq. (10):

$$182 \quad \lambda_{sen} = \lambda_{ref} + \int_{T_{ref}}^T C_p dT \quad (10)$$

183 Where  $c_p$  is the specific heat at constant pressure, and  $\lambda_{ref}$  is the enthalpy at the  
 184 reference temperature ( $T_{ref} = 293.15$  K). The variation in enthalpy in the phase change  
 185 ( $\lambda_L$ ) is a function of temperature, obtained by Eq. (11) or by Eq. (12)

$$186 \quad \lambda_L = \gamma L \quad (11)$$

$$187 \quad \lambda_L = \begin{cases} 0 & \text{if } T < T_s \\ L & \text{if } T > T_l \\ \gamma L & \text{if } T_s < T < T_l \end{cases} \quad (12)$$

## 188 2.2 Initial and Boundary Conditions

189 The initial conditions consisted of  $V(x, y, 0) = 0$  and  $T(x, y, 0) = 20^\circ\text{C}$ . The  
190 boundary conditions used were:

$$191 \quad T|_{r=R_{in}} = T_w \quad V|_{r=R_{in}} = 0 \quad (13)$$

$$192 \quad q''|_{r=R_{ex}} = 0 \quad V|_{r=R_{ex}} = 0 \quad (14)$$

193 where  $T_w = 80^\circ\text{C}$  and  $q''_w$  are the temperature and the heat flow in the wall,  
194 respectively. The following boundary conditions were considered in the fin walls:

$$195 \quad T = T_w = 80^\circ\text{C} \text{ and } V = 0 \quad (15)$$

## 196 2.3 Numerical Method and Validation

197 The simulations were performed in ANSYS Fluent software 18.2. The pressure  
198 was defined as *PRESTO*, the *SIMPLE* method was used for the pressure-velocity  
199 coupling and the gradient of spatial discretization as *Least Squares Cell-Based*. The  
200 relaxation factors used for pressure, density, field forces, momentum, liquid fraction,  
201 and energy were, respectively: 0.3; 1.0; 0.5; 0.5; 0.6 and 1.0. The energy and  
202 momentum were established as *Second-Order Upwind*. With a limit of 1000  
203 interactions per time step, the time step was 0.01 s. The absolute convergence criterion  
204 established was  $10^{-6}$  for mass and velocity and  $10^{-8}$  for the energy equation.

205 The continuous growth of publications related to CFD and the significant  
206 advances in computational techniques and technologies have also improved methods  
207 for validating results, ensuring the credibility of works involving computational fluid  
208 dynamics. Among the mesh validation methods, GCI (Grid Convergence Index) is  
209 credible and recommended, having been proven through hundreds of cases [33].  
210 Three computational meshes were created (*M1*, *M2*, *M3*), with 28457, 14520, and  
211 10118 volumes respectively, applying this methodology. GCI was calculated for each  
212 mesh and evaluated. For *M1*, GCI had an average value of 0.003%, affirming the

213 quality of this mesh. Mesh *M1* is composed of quadrilateral elements and is shown in  
214 Fig. 3. Also seen in Fig. 3 is the great mesh refinement in active surfaces: Detail (A)  
215 shows the refining gradient on the fin walls while Detail (B) shows the refinement of  
216 the elements close to the inner cylinder wall. All meshes used in the study of fin aspect  
217 ratio followed the same criteria of distribution and refinement of the elements.

218 For numerical validation, experimental data of Al-Abidi et al. [34] and  
219 Yuan et al. [23] were used. Both cases are for an annular heat exchanger with internal  
220 fins, filled with PCM. Quantitative analysis of the Al-Abidi et al. [34] data was performed  
221 using the values of local temperature ( $T$ ) as a time ( $t$ ) function. Fig. 4 shows an  
222 approximate temperature behavior between the present work and the experimental  
223 data. The average percentage difference between both is 4.9%. This is a relatively  
224 small difference because it is a local temperature value. Quantitative analysis of the  
225 Yuan et al. [23] data was performed using the values of the liquid fraction ( $\beta$ ) as a  
226 function of the Fourier number ( $Fo = \alpha t / L_c^2$ ), where  $\alpha = 7.53 \cdot 10^{-8} \text{ m}^2/\text{s}$  is the thermal  
227 diffusivity, and  $L_c = 0.04 \text{ m}$  is the characteristic length established by the author. A  
228 comparison of the results obtained by this work and those presented by the reference  
229 are shown in Fig. 5. It presents an average percentage difference of approximately  
230 1.5%, which proves a good agreement between results.

231 Qualitative analysis comparing the results from this work and Yuan et al. [23] is  
232 shown in Figs. 6(a-b), respectively. The figures present the  $\beta$  fields at different melting  
233 stages, where the blue and red represent the solid and the liquid phase of the PCM,  
234 respectively. Regardless of running time, the similarity between results was significant,  
235 showing the satisfactory agreement of the numerical model.

236 As previously presented, the mesh analysis revealed a very low GCI, giving  
237 credibility to the results. A triple validation with experimental data from two different  
238 authors was presented. In view of the great results obtained, the model was considered  
239 validated and adequate for the case study.

### 240 3 Results and Discussions

241 In the initial moments of the melting process, heat transfer is predominantly  
242 through conduction due to the solid layer's direct contact with the heated wall. As the  
243 liquid layer forms between the heated wall and the solid, the participation of natural  
244 convection in the heat transfer process increases. This process is shown in Figs. 7(a-

245 b) for  $AR = 7/8$  and  $\phi = 0.003$  in systems with vertical and horizontal fins, respectively.  
 246 The right side of the section shows streamlines, and the left side shows temperature  
 247 fields. The streamlines are superimposed on the liquid fraction plane, where the black  
 248 color indicates the solid phase and white the liquid phase. The Details shown in Figs.  
 249 7(c-h) present the velocity vectors.

250 The left side of Figs. 7(a-b) shows contours of the temperature of the phase-  
 251 change process. In the vertical fin geometry of Fig. 7(a), a temperature gradient can  
 252 be seen in the solid phase (blue to yellow/green). This gradient occurs because the  
 253 PCM is sub-cooled at the initial condition. In the liquid region (red), horizontal thermal  
 254 stratification is observed. Temperature gradients are also seen close to the solid-liquid  
 255 interface and the internal wall of the exchanger, depicting a tendency of upward drag  
 256 along the internal and descending walls and near the solid-liquid interface. This  
 257 behavior is confirmed in the vectors shown in Figs. 7(c-d), where ascending and  
 258 descending convective currents can be observed. Upward convective currents are a  
 259 direct result of the buoyancy from the reduction of the PCM density as the internal  
 260 surface of the exchanger is heated concerning the PCM. Note that a downward  
 261 convective current must also be present to preserve the conservation of the mass, as  
 262 verified.

263 In this work, the number of Rayleigh was defined as  $Ra =$   
 264  $[g \zeta L_c^3 (T_w - T_m)] / (\nu \alpha)$ , where  $\nu$  is the kinematic viscosity. Since the temperature  
 265 and the characteristic length ( $L_c = R_{ext}$ ) are the same for all cases studied,  $Ra = 34364$ .  
 266 This value is greater than the critical Rayleigh ( $Ra_{cr} = 12250$ ) presented by Yigit et al.  
 267 [35], to an equivalent annular geometry, which justifies the appearance of Rayleigh-  
 268 Bénard cells. In the horizontal fin geometry of Fig. 7(b) temperature contours also show  
 269 a thermal gradient in the solid phase as per the initial sub-cooled state. However, the  
 270 liquid phase has a diffuse temperature gradient. Such behavior is following the  
 271 expected Rayleigh-Bénard convective behavior of a heated surface. This fact becomes  
 272 evident from characteristic recirculations of the Rayleigh-Bénard behavior shown by  
 273 the streamlines over the horizontal heated surfaces, as well as vectors of Figs. 7(e, g).  
 274 In this convective process, the heated liquid rises in multiple regions perpendicular to  
 275 the heat source, coming into contact and fusing the solid interface as it exchanges heat  
 276 and cools. Due to the conservation of mass, cooled liquid moves downwards towards  
 277 the heated plane, establishing a recirculation zone and an efficient thermal exchange  
 278 cycle. Fig. 7(f) shows an upward flow near the heated surface of the tube and

279 consequently, downward flow due to the presence of Rayleigh-Bénard cells at the top  
 280 of the cavity. The shear region between ascending and descending flows can also be  
 281 seen in Fig. 7(h). This resulting intense thermal exchange system persists if there is a  
 282 solid material in the region above the heated surfaces.

283 The evolution of the melting process for a sample of the studied cases is shown  
 284 in Figs. 8(a-e), where the liquid-solid interfaces can be observed at 1 min, 10 min, 20  
 285 min, 30 min, 40 min, and 60 min. It is possible to observe the progress of cases with  
 286  $AR = 1/4$ ,  $1/2$  and  $7/8$  for all  $\phi$ , both in terms of melting and the geometric aspect  
 287 evolution with the variation of  $AR$  and  $\phi$ . The first three columns cover cases with  
 288 vertical fins, while the last three refer to cases with horizontal fins. Observing the lines  
 289 for horizontal fins at  $t = 1$  min, 10 min, and 20 min, the liquid region advances  
 290 significantly in comparison to the respective cases with vertical fins. This trend is in line  
 291 with the natural convection process shown in Fig. 7.

292 The liquid fraction lines of Figs. 8(a-e) at  $t = 30$  min, 40 min, and 60 min show a  
 293 deceleration in the melting speed of the cases with horizontal fins compared to vertical  
 294 fins as the solid phase moves away from heated surfaces. It is noted that the total  
 295 melting process concluded before 40 min for the vertical fin, while for the horizontal fin,  
 296 the melting process extends beyond the 60 min when analyzing specifically the cases  
 297 with  $AR = 7/8$  of Fig. 8(e).

298 **Figures 9(a-e)** shows the variation of  $\beta$  vs. Fourier number ( $Fo = \alpha t/L_c^2$ ), for  
 299 horizontal and vertical fins with  $AR = 7/8$ ,  $3/4$ ,  $1/2$ ,  $1/4$ , and  $1/8$  for  $\phi = 0.003$ ,  $0.005$ ,  
 300  $0.01$ ,  $0.02$ , and  $0.03$ . In this work, the characteristic length was defined as  $L_c = R_{ext}$ .  
 301 **Figures 9(a-e)** shows that for all cases up to approximately  $Fo = 0.006$ , the values of  
 302  $\beta$  are practically superimposed before drifting apart as  $Fo$  increases. Between  
 303  $Fo = 0.006$  and  $Fo = 0.05$ , melting is favored by horizontal fins, with the faster melting  
 304 process occurring in the fin with  $AR = 7/8$  for all the values of  $\phi$ . From  $Fo = 0.05$  and  
 305 higher, there is a transition in the slope of the horizontal fins, with the reduction of the  
 306 melting rate in these configurations. Afterward, vertical fins complete the melting  
 307 process ahead of horizontal fins starting from the highest  $AR = 7/8$  and proceeding in  
 308 an orderly way to the lowest  $AR = 1/8$ . Only after the total melting of all cases with  
 309 vertically oriented fins, the cases with horizontally oriented fins begin to reach  $\beta = 1$ ,  
 310 also in an orderly manner, from the cases with the highest  $AR$ , down to the lowest.  
 311 **This behavior of  $\beta$  is similar for all  $\phi$  values, with only a subtle increase in the melting**  
 312 **rate as  $\phi$  increases.**

313 Figures 10(a-c) present the liquid fraction fields (right side) and temperature  
 314 fields (left side) at  $t = 600$  s and  $2270$  s, for  $\phi = 0.03$  and  $AR = 7/8, 1/2$  and  $1/4$ ,  
 315 respectively. The initial instant ( $600$  s) enables us to view the heat exchange  
 316 mechanisms present at the beginning of the melting process, while the final instant  
 317 ( $2270$  s) refers to the total melting time of the fastest case (vertical fins with  $AR = 7/8$ ).  
 318 This observation allows a comparison of the other cases melting state at the same  
 319 instant as when the fastest case had already concluded. The  $\beta$  value is displayed at  
 320 the center of each geometry. Observing the temperature fields at  $t = 600$  s, it is visible  
 321 the greater dynamism of the cases with horizontal fins as the weaving outlines are  
 322 consistent with recirculations of the Rayleigh-Bénard convective behavior. In contrast,  
 323 in the cases with vertically oriented fins, it is possible to observe relatively stratified  
 324 temperature fields and upward flow behavior only in the region close to the fins and  
 325 the heated wall. Consequently, the  $\beta$  value is higher for cases with horizontal fins.

326 Still, concerning Figs. 10(a-c) at  $t = 2270$  s, it can be seen in all cases that the  
 327 temperature fields show a well-defined thermal step between solid and liquid phase  
 328 despite presenting a small thermal stratification close to the solid-liquid interface.  
 329 However, when comparing the  $\beta$  values between vertical and horizontal fins, it is  
 330 observed that the vertical fins have a higher melting rate than the horizontal fins  
 331 because the vertical fins are closer to the solid mass, compared to the horizontal fins.

332 **Figures 11(a-e)** shows the behavior of the Nusselt number ( $\overline{Nu} = \bar{h} \cdot L_c / k_l$ ) as  
 333 a function of  $Fo$ , for horizontal and vertical fins with  $AR = 7/8, 3/4, 1/2, 1/4$ , and  $1/8$  for  
 334  $\phi = 0.003, 0.005, 0.01, 0.02$ , and  $0.03$ . The average heat transfer coefficient  
 335  $[\bar{h} = q'' / (T_w - T_m)]$  is calculated from is the total heat flow ( $q''$ ) while the temperatures  
 336 are taken as  $T_w = 80^\circ\text{C}$  at the active wall and  $T_m = 44.2^\circ\text{C}$  as the melting temperature  
 337 of the PCM. **Figures 11(a-e)** can be divided into three behavior patterns indicated by I,  
 338 II, and III. As observed by Ji et al. [26], these patterns are related to the heat exchange  
 339 mechanisms during the phase change of the PCM. **In addition to the analysis of  $Nu$**   
 340 **values, Figs. 12(a-c) shows the fields of temperature, liquid fraction, and streamlines**  
 341 **of an example case. The joint analysis of Figs. 11(a-e) with Figs. 12(a-c) allows better**  
 342 **compression of the three-behavior described below.** Region I start with  $\overline{Nu}$  higher than  
 343 12 for all cases. This fact is due to the process beginning when there is direct contact  
 344 between the solid PCM and the heat source. As the PCM melts, the liquid interface is  
 345 formed between the solid and the heat source. The increasing size of the liquid layer

346 increases the thermal resistance by conduction between the heated wall and the  
 347 melting material with a gradual decrease to  $Fo = 0.003$ , as can be observed in the  
 348 Fig. 12(a). Region II is characterized by the beginning of fluctuations in the behavior of  
 349  $\overline{Nu}$ . These fluctuations are due to a further increase in the liquid layer's size and the  
 350 beginning of an intense convective process, which can be observed in the streamlines  
 351 of the Fig. 12(b). The greater dynamism of the convective process on the horizontally  
 352 oriented fins, its due the Rayleigh-Bénard convective pattern. In line with this  
 353 phenomenon, the highest values of  $\overline{Nu}$  that occur in this region are relative to the  
 354 horizontal fins (dashed lines). In region III, from  $Fo = 0.05$ ,  $\overline{Nu}$  decreases rapidly for  
 355 cases with a horizontal fin. As shown in Fig. 12(c), this behavior makes the heat  
 356 transfer process restricted to a practically conductive in the molten and stationary  
 357 liquid. As the melting process approaches the end, cases with vertically oriented fins  
 358 presents a gradual drop in the value of  $\overline{Nu}$ , until zero. This behavior of  $Nu$  is similar for  
 359 all  $\phi$  values, with only a subtle increase in region II, according to the increase in  $\phi$ .

360 One way to qualify the different systems analyzed is by their effectiveness ( $\eta_f$ )  
 361 in relation to the system without fins. In this work, this effectiveness is defined as:  $\eta_f =$   
 362  $(\beta/\beta_0) - 1$ , where  $\beta_0$  is the liquid fraction of a case without fins at the same instant in  
 363 time. Figures 13(a-e) shows the variation of  $\eta_f$  as a function of  $Fo$  for vertical and  
 364 horizontal fins with  $AR = 1/8, 1/4, 1/2, 3/4,$  and  $7/8$  for  $\phi = 0.003, 0.005, 0.01, 0.02,$  and  
 365  $0.03$ . It is initially observed that all cases present their highest  $\eta_f$  at the beginning of the  
 366 melting process. Ideally,  $\eta_f$  would remain high throughout the melting process.  
 367 However, the cases show two patterns of decrease, first more accentuated and then  
 368 gradually. The effectiveness of horizontal and vertical fins, represented by dotted and  
 369 continuous lines, respectively, is quantitatively similar for each value of  $AR$ . The value  
 370 of  $\eta_f$  is initially higher for horizontal fins, but for  $Fo > 0.06$ , vertical fins become more  
 371 efficient. This inversion occurs for all  $AR$  presented. Horizontal fins have  $\eta_f$  tending to  
 372 0 with increasing  $Fo$ . This tendency indicates the fins' inefficiency in the melting  
 373 process since the null value of  $\eta_f$  is equivalent to a system without fins. However,  
 374 vertical fins keep the  $\eta_f$  value practically stable between  $Fo = 0.06$  and the ending of  
 375 the melting process. For these geometries, higher  $AR$  values reveal greater  
 376 effectiveness and lower  $Fo$  value after the melting process. The  $\eta_f$  behavior is  
 377 equivalent to all  $\phi$  values, with a directly proportional increase between the  $\eta_f$  and  $\phi$   
 378 values.

379 Figures 14(a-b) show the time to reach complete melting ( $t_m$ ) as a function of  
 380  $AR$ , for horizontal and vertical fins, respectively, with  $\phi = 0.003, 0.005, 0.01, 0.02$  and  
 381  $0.03$ . For better visualization of the results, the  $t_m$  range is different between the cases.  
 382 Figures 14(a-b) shows that for both horizontal and vertical fins, the decrease in  $t_m$  is  
 383 practically linear with  $AR$ .

384 For cases with horizontal fins, Fig. 14(a) shows a decrease in  $t_m$  with an increase  
 385 in  $AR$  below 1000 s for all values of  $\phi$ . This small period indicates the low  
 386 representativeness of the aspect ratio in the total melting time when the fins are  
 387 arranged horizontally. This fact is related to what is observed in Figs. 13(a-e), where it  
 388 can be observed that  $\eta_f$  is practically null, for all  $AR$  values at the end of the melting  
 389 process of the cases with horizontal fins. Even if cases with horizontal fins promote a  
 390 higher melting rate at the beginning of the process, the conclusion of the melting  
 391 process stretches further due to the gap between the solid PCM and the heat source.  
 392 Increases in  $AR$  in horizontal fins do not reduce this gap.

393 The total melting time of cases with vertical fins of Fig. 14(b) varies between  
 394 2000 s and 8000 s. The higher amplitude in this ordinate axis is due to the more  
 395 significant influence of the  $AR$  variation on the total melting time. As seen in Figs. 13(a-  
 396 e), the increase in  $AR$  results in greater effectiveness at the end of the melting process  
 397 for vertical fins. Since vertical fins maintain proximity between the heat source and the  
 398 solid PCM until the end of the melting process, increases in  $AR$  also increase the  
 399 proximity of the heated wall to the solid PCM.

400 As seen in Figs. 14(a-b), the shortest total melting time ( $t_{m,min}$ ) occurs for  
 401  $AR = 0.88$  (7/8). In these figures, although the tendency of  $t_{m,min}$  to decrease with  
 402 increasing  $\phi$  can be observed, a more accurate assessment is shown in Figs. 15(a-b),  
 403 which show the variation of  $t_{m,min}$  as a function of  $\phi$ , for horizontal and vertical fins,  
 404 respectively, at the shortest melting time of  $AR = 0.88$ . Figures 15(a-b) demonstrate  
 405 that  $t_{m,min}$  is inversely proportional to  $\phi$  regardless of the fin layout. This can be due to  
 406 the volume reduction of PCM in the cavity since the increase in  $\phi$  implies an increase  
 407 in the volume occupied by the fin. It is also observed that the range of variation of  $t_{m,min}$   
 408 is higher for vertical fins (Fig.15(b)) than for horizontal fins (Fig. 15(a)). The difference  
 409 between the time ranges is the result of prolonged load cycles in systems with  
 410 horizontal fins and shorter cycles in systems with vertical fins, as seen in Figs. 14(a-  
 411 b).

## 412 5 Conclusions

413 This work sought to analyze the behavior of the melting process of lauric acid  
414 PCM in a cylindrical cavity concerning the dimensional variation fins. The numerical  
415 model was validated with numerical and experimental results provided by literature.  
416 The computational mesh analysis was performed using the GCI method, which  
417 resulted in an average value of 0.003%. Under these conditions, the main results were:

- 418 • Horizontal fins had a melting rate up to 15% higher than vertical fins if there was  
419 solid PCM in the region above the layer of PCM already fused next to the horizontal  
420 fin. This occurred for all values of  $\phi$  and was due to localized Rayleigh-Bénard  
421 convective effect;
- 422 • For all values of  $\phi$ , the total time for complete melting was, on average, 44% lower  
423 for vertical fins than for horizontal fins. In a vertical fin configuration, buoyancy  
424 effects were less pronounced in the active wall (circular internal) and the vertical  
425 fin. Consequently, this region was the last to be melted, and higher temperature  
426 differences develop between PCM and active walls, promoting higher rates of heat  
427 transfer throughout the melting process;
- 428 • Increases of the aspect ratio, or thinness, of the fin, reduced the time of the total  
429 melting process by the maximum values of 11.3% for vertical fins and 1.2% for  
430 horizontal fins, with  $\phi = 0.003$ ;
- 431 • Increases in  $\phi$  resulted in an approximately linear decrease in the total melting time  
432 of the PCM in the heat exchanger. This was due to the larger area of the fin's  
433 occupancy in the cavity.

434

## 435 Acknowledgments

436 We thank FAPERGS (Research Support Foundation of the State of Rio Grande do  
437 Sul – Process: 2270-25.51/14-8), The National Council of Scientific and Technological  
438 Development (CNPq – Process: 307791/2019-0), and the Italian Ministry for  
439 Education, University and Research, for their support in carrying out this research.

440

441

## REFERENCES

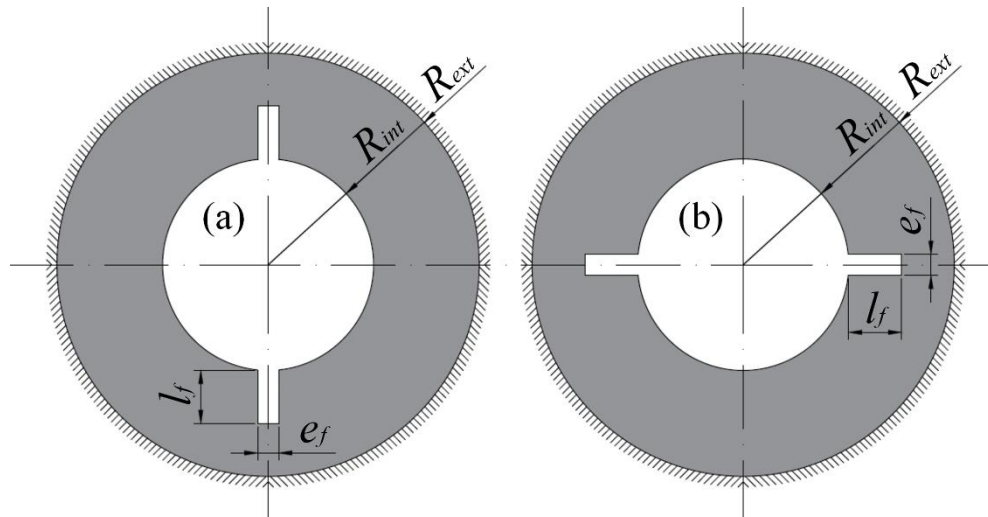
442 [1] L. Kalapala, J.K. Devanuri, Influence of operational and design parameters on

- 443 the performance of a PCM based heat exchanger for thermal energy storage –  
444 A review, *J. Energy Storage*. 20 (2018) 497–519.
- 445 [2] G. Alva, Y. Lin, G. Fang, An overview of thermal energy storage systems,  
446 *Energy*. 144 (2018) 341–378. <https://doi.org/10.1016/j.energy.2017.12.037>.
- 447 [3] J. Jaguemont, N. Omar, P. Van den Bossche, J. Mierlo, Phase-change materials  
448 (PCM) for automotive applications: A review, *Appl. Therm. Eng.* 132 (2018) 308–  
449 320. <https://doi.org/10.1016/j.applthermaleng.2017.12.097>.
- 450 [4] R. VELRAJ, R. V. SEENIRAJ, B. HAFNER, C. FABER, K. SCHWARZER,  
451 Experimental analysis and numerical modelling of inward solidification on a  
452 finned vertical tube for a latent heat storage unit, *Sol. Energy*. 60 (1997) 281–  
453 290.
- 454 [5] M.N.A. Hawlader, M.S. Uddin, M. Mya, Microencapsulated PCM thermal-energy  
455 storage system, *Appl. Energy*. 74 (2003) 195–202.
- 456 [6] J.P. Trelles, J.J. Dufly, Numerical simulation of porous latent heat thermal energy  
457 storage for thermoelectric cooling, *Appl. Therm. Eng.* 23 (2003) 1647–1664.  
458 [https://doi.org/10.1016/S1359-4311\(03\)00108-X](https://doi.org/10.1016/S1359-4311(03)00108-X).
- 459 [7] E.S. Mettawee, G.M.R. Assassa, Thermal conductivity enhancement in a latent  
460 heat storage system, *Sol. Energy*. 81 (2007) 839–845.  
461 <https://doi.org/10.1016/j.solener.2006.11.009>.
- 462 [8] S.F. Hosseinizadeh, A.A.R. Darzi, F.L. Tan, Numerical investigations of  
463 unconstrained melting of nano-enhanced phase change material ( NEPCM )  
464 inside a spherical container, *Int. J. Therm. Sci.* 51 (2012) 77–83.  
465 <https://doi.org/10.1016/j.ijthermalsci.2011.08.006>.
- 466 [9] A. Sari, K. Kaygusuz, Thermal performance of a eutectic mixture of lauric and  
467 stearic acids as PCM encapsulated in the annulus of two concentric pipes, *Sol.*  
468 *Energy*. 72 (2002) 493–504.
- 469 [10] A. Atal, Y. Wang, M. Harsha, S. Sengupta, Effect of porosity of conducting matrix  
470 on a phase change energy storage device, *Int. J. Heat Mass Transf.* 93 (2016)  
471 9–16. <https://doi.org/10.1016/j.ijheatmasstransfer.2015.09.033>.
- 472 [11] F. Agyenim, P. Eames, M. Smyth, Heat transfer enhancement in medium  
473 temperature thermal energy storage system using a multitube heat transfer  
474 array, *Renew. Energy*. 35 (2010) 198–207.  
475 <https://doi.org/10.1016/j.renene.2009.03.010>.
- 476 [12] A.M. Abdulateef, S. Mat, J. Abdulateef, K. Sopian, A.A. Al-Abidi, Geometric and

- 477 design parameters of fins employed for enhancing thermal energy storage  
478 systems: a review, *Renew. Sustain. Energy Rev.* 82 (2018) 1620–1635.  
479 <https://doi.org/10.1016/j.rser.2017.07.009>.
- 480 [13] A.R. Darzi, M. Farhadi, K. Sedighi, Numerical study of melting inside concentric  
481 and eccentric horizontal annulus, *Appl. Math. Model.* 36 (2012) 4080–4086.  
482 <https://doi.org/10.1016/j.apm.2011.11.033>.
- 483 [14] Y. Pahamli, M.J. Hosseini, A.A. Ranjbar, R. Bahrampoury, Inner pipe downward  
484 movement effect on melting of PCM in a double pipe heat exchanger, *Appl. Math.*  
485 *Comput.* 316 (2018) 30–42. <https://doi.org/10.1016/j.amc.2017.07.066>.
- 486 [15] Y. Pahamli, M.J. Hosseini, A.A. Ranjbar, R. Bahrampoury, Analysis of the effect  
487 of eccentricity and operational parameters in PCM-filled single-pass shell and  
488 tube heat exchangers, *Renew. Energy.* 97 (2016) 344–357.  
489 <https://doi.org/10.1016/j.renene.2016.05.090>.
- 490 [16] A. a. Al-Abidi, S. Mat, K. Sopian, M.Y. Sulaiman, A.T. Mohammad, Numerical  
491 study of PCM solidification in a triplex tube heat exchanger with internal and  
492 external fins, *Int. J. Heat Mass Transf.* 61 (2013) 684–695.  
493 <https://doi.org/10.1016/j.ijheatmasstransfer.2013.02.030>.
- 494 [17] S. Mat, A.A. Al-abidi, K. Sopian, M.Y. Sulaiman, A. Th, Enhance heat transfer  
495 for PCM melting in triplex tube with internal – external fins, *Energy Convers.*  
496 *Manag.* 74 (2013) 223–236.
- 497 [18] M.K. Rathod, J. Banerjee, Thermal performance enhancement of shell and tube  
498 Latent Heat Storage Unit using longitudinal fins, *Appl. Therm. Eng.* 75 (2015)  
499 1084–1092. <https://doi.org/10.1016/j.applthermaleng.2014.10.074>.
- 500 [19] A.M. Abdulateef, S. Mat, K. Sopian, J. Abdulateef, A.A. Gitan, Experimental and  
501 computational study of melting phase-change material in a triplex tube heat  
502 exchanger with longitudinal/triangular fins, *Sol. Energy.* 155 (2017) 142–153.  
503 <https://doi.org/10.1016/j.solener.2017.06.024>.
- 504 [20] A. Sciacovelli, F. Gagliardi, V. Verda, Maximization of performance of a PCM  
505 latent heat storage system with innovative fins, *Appl. Energy.* 137 (2015) 707–  
506 715. <https://doi.org/10.1016/j.apenergy.2014.07.015>.
- 507 [21] A.A. Rabienataj Darzi, M. Jourabian, M. Farhadi, Melting and solidification of  
508 PCM enhanced by radial conductive fins and nanoparticles in cylindrical annulus,  
509 *Energy Convers. Manag.* 118 (2016) 253–263.  
510 <https://doi.org/10.1016/j.enconman.2016.04.016>.

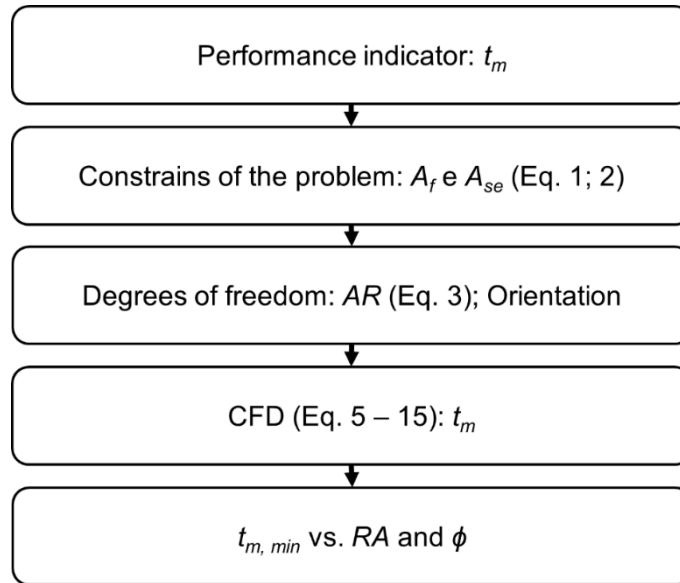
- 511 [22] P. Wang, H. Yao, Z. Lan, Z. Peng, Y. Huang, Y. Ding, Numerical investigation of  
512 PCM melting process in sleeve tube with internal fins, *Energy Convers. Manag.*  
513 110 (2016) 428–435. <https://doi.org/10.1016/j.enconman.2015.12.042>.
- 514 [23] Y. Yuan, X. Cao, B. Xiang, Y. Du, Effect of installation angle of fins on melting  
515 characteristics of annular unit for latent heat thermal energy storage, *Sol.*  
516 *Energy.* 136 (2016) 365–378. <https://doi.org/10.1016/j.solener.2016.07.014>.
- 517 [24] J.M. Mahdi, E.C. Nsofor, Melting enhancement in triplex-tube latent thermal  
518 energy storage system using nanoparticles-fins combination, *Int. J. Heat Mass*  
519 *Transf.* 109. 109 (2017) 417–427.  
520 <https://doi.org/10.1615/TFEC2017.est.018280>.
- 521 [25] J.M. Mahdi, E.C. Nsofor, Solidification enhancement of PCM in a triplex-tube  
522 thermal energy storage system with nanoparticles and fins, *Appl. Energy.* 211  
523 (2018) 975–986.
- 524 [26] C. Ji, Z. Qin, S. Dubey, F.H. Choo, F. Duan, Simulation on PCM melting  
525 enhancement with double-fin length arrangements in a rectangular enclosure  
526 induced by natural convection, *Int. J. Heat Mass Transf.* 127 (2018) 255–265.  
527 <https://doi.org/10.1016/j.ijheatmasstransfer.2018.07.118>.
- 528 [27] S. Deng, C. Nie, G. Wei, W.B. Ye, Improving the melting performance of a  
529 horizontal shell-tube latent-heat thermal energy storage unit using local  
530 enhanced finned tube, *Energy Build.* 183 (2019) 161–173.  
531 <https://doi.org/10.1016/j.enbuild.2018.11.018>.
- 532 [28] Jasim M. Mahdi, Sina Lohrasbi, Davood D. Ganji, Emmanuel C. Nsofor,  
533 Accelerated melting of PCM in energy storage systems via novel configuration  
534 of fins in the triplex-tube heat exchanger, *Int. J. Heat Mass Transf.* 124 (2018)  
535 663–676. <https://doi.org/10.1016/j.ijheatmasstransfer.2018.03.095>.
- 536 [29] J.M. Mahdi, S. Lohrasbi, D.D. Ganji, E.C. Nsofor, Simultaneous energy storage  
537 and recovery in the triplex-tube heat exchanger with PCM, copper fins and Al<sub>2</sub>  
538 O<sub>3</sub> nanoparticles, *Energy Convers. Manag.* 180 (2019) 949–961.
- 539 [30] S. POLAT, P. SAYAN, Kinetic analysis and polymorphic phase transformation of  
540 glycine in the presence of lauric acid, *J. Cryst. Growth.* 481 (2018) 71–79.  
541 <https://doi.org/10.1016/j.jcrysgr.2017.10.037>.
- 542 [31] A. Sarı, K. Kaygusuz, Thermal and heat transfer characteristics in a latent heat  
543 storage system using lauric acid Sar, A. and Kaygusuz, K. *Energy Conversion*  
544 *and Management*, 2002, 43, (18), 2493–2507, *Fuel Energy Abstr.* 44 (2003)

- 545 189–190. [https://doi.org/10.1016/S0140-6701\(03\)82063-5](https://doi.org/10.1016/S0140-6701(03)82063-5).
- 546 [32] V.R. Voller, C. Prakash, A fixed grid numerical modelling methodology for  
547 convection-diffusion mushy region phase-change problems, *Int. J. Heat Mass*  
548 *Transf.* 30 (1987) 1709–1719. [https://doi.org/10.1016/0017-9310\(87\)90317-6](https://doi.org/10.1016/0017-9310(87)90317-6).
- 549 [33] I.B. Celik, U. Ghia, P.J. Roache, C.J. Freitas, H. Coleman, P.E. Raad, Procedure  
550 for Estimation and Reporting of Uncertainty Due to Discretization in CFD  
551 Applications, *J. Fluids Eng.* 130 (2008) 078001.  
552 <https://doi.org/10.1115/1.2960953>.
- 553 [34] A.A. Al-Abidi, S. Mat, K. Sopian, M.Y. Sulaiman, A.T. Mohammad, Internal and  
554 external fin heat transfer enhancement technique for latent heat thermal energy  
555 storage in triplex tube heat exchangers, *Appl. Therm. Eng.* 53 (2013) 147–156.  
556 <https://doi.org/10.1016/j.applthermaleng.2013.01.011>.
- 557 [35] S. Yigit, N. Chakraborty, Numerical investigation of aspect ratio influences on  
558 Rayleigh-Bénard convection of power-law fluids in vertical cylindrical annuli,  
559 *Therm. Sci. Eng. Prog.* 9 (2019) 185–199.  
560 <https://doi.org/10.1016/j.tsep.2018.10.007>.
- 561



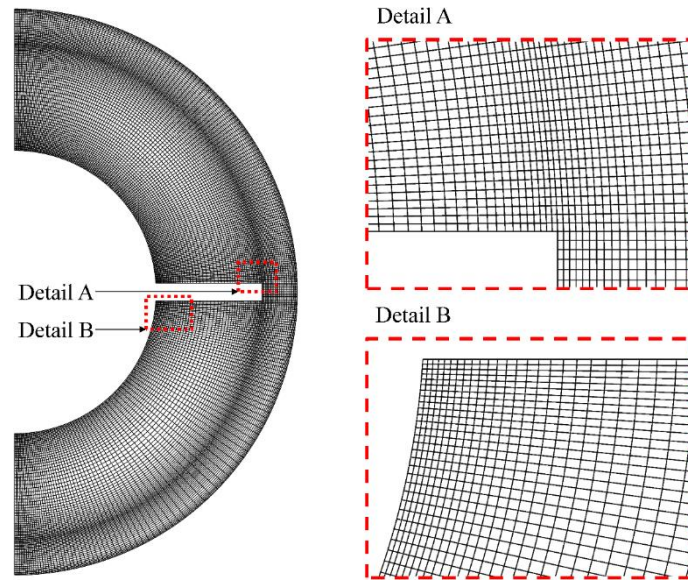
562

Figure 1 - Annular tube with: (a) vertical and (b) horizontal fins.

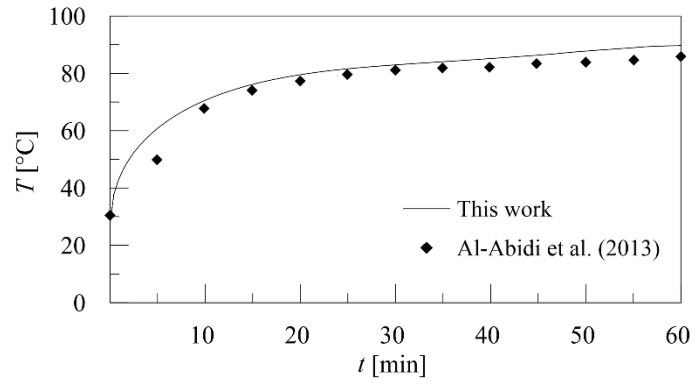


563

Figure 2 – Flowchart of fin studies conducted.



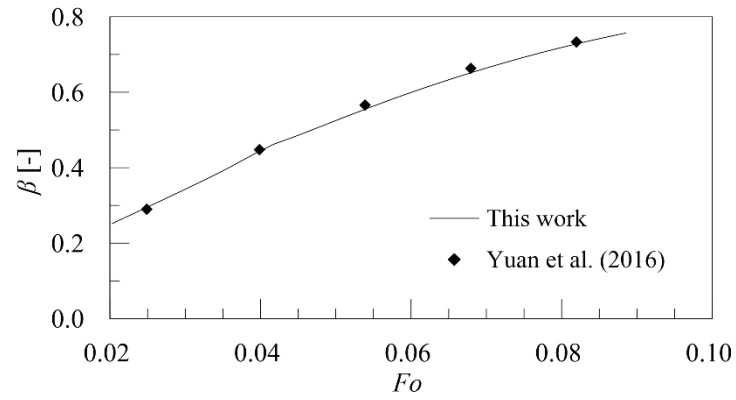
564 Figure 3 – Computational mesh with details at the fin end (A) and the fin base and  
565 inner cylinder wall (B).



566

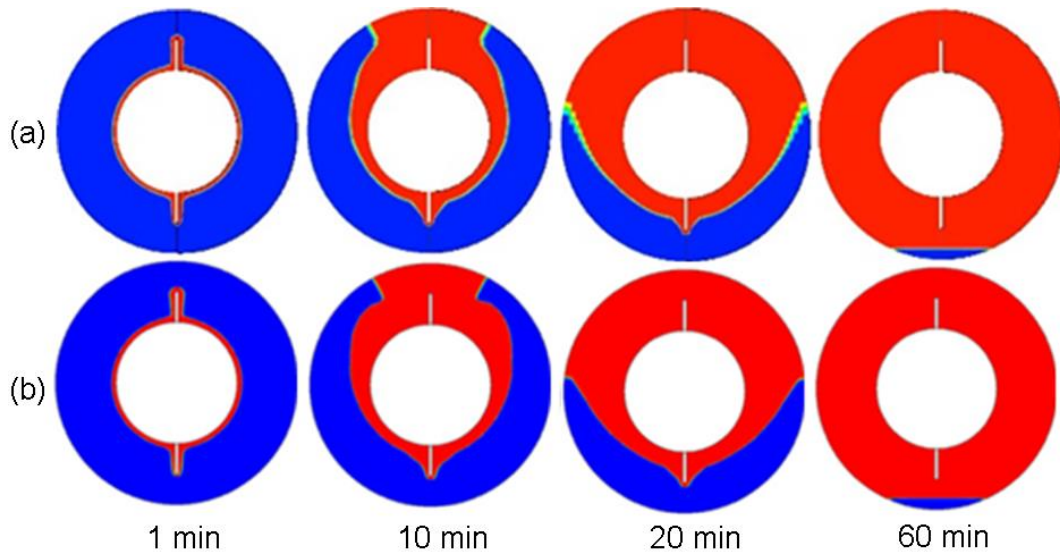
Figure 4 – Temperature ( $T$ ) vs. ( $t$ ): current numerical simulation and experimental data from Al-Abidi et al. [23].

567



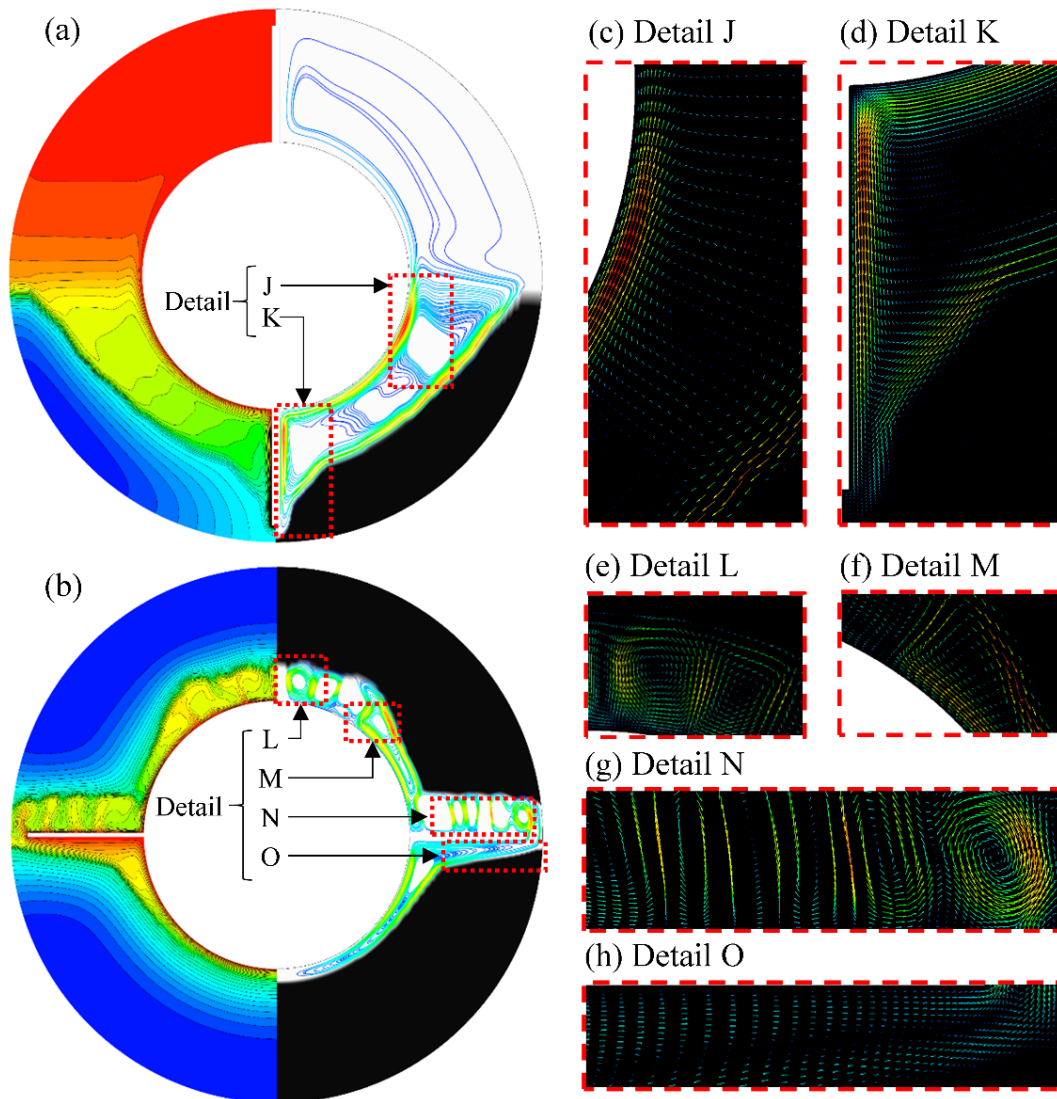
568 Figure 5 – Liquid fraction ( $\beta$ ) vs.  $Fo$ : current numerical simulation and experimental  
569 data from Yuan et al. [23].

570



571

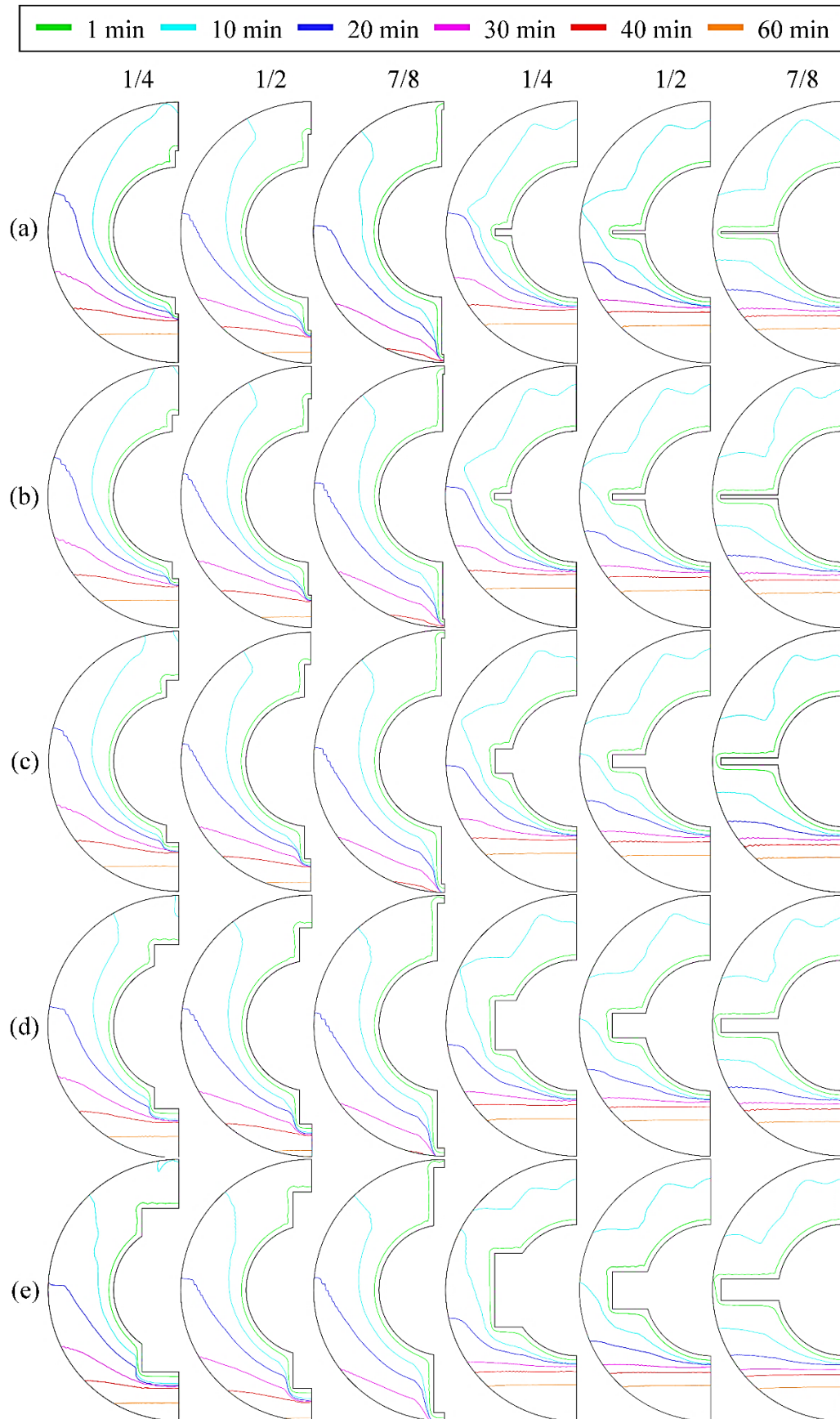
572 Figure 6  $-\beta$  fields at  $t = 1; 10; 20$  and  $60$  min: (a) current numerical simulation and (b)  
573 experimental data from Yuan et al. [23].



574

575  
576  
577

Figure 7 – T fields and streamlines, with details of the velocity vectors for  $AR = 7/8$  and  $\phi = 0.003$ : (a) vertical fins, (b) horizontal fins and (c, d, e, f, g, h) related to Details J, K, L, M, N and O respectively.

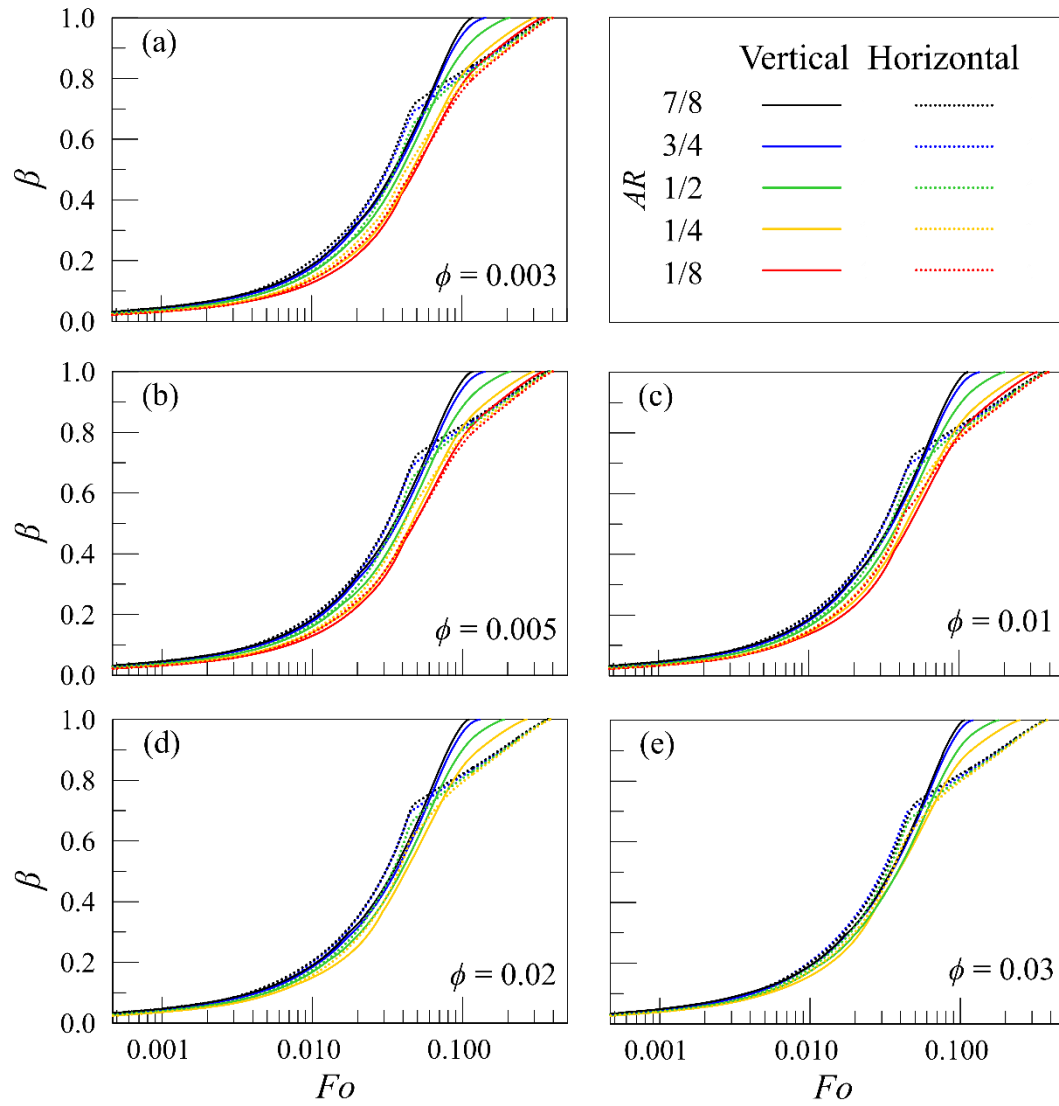


578

579

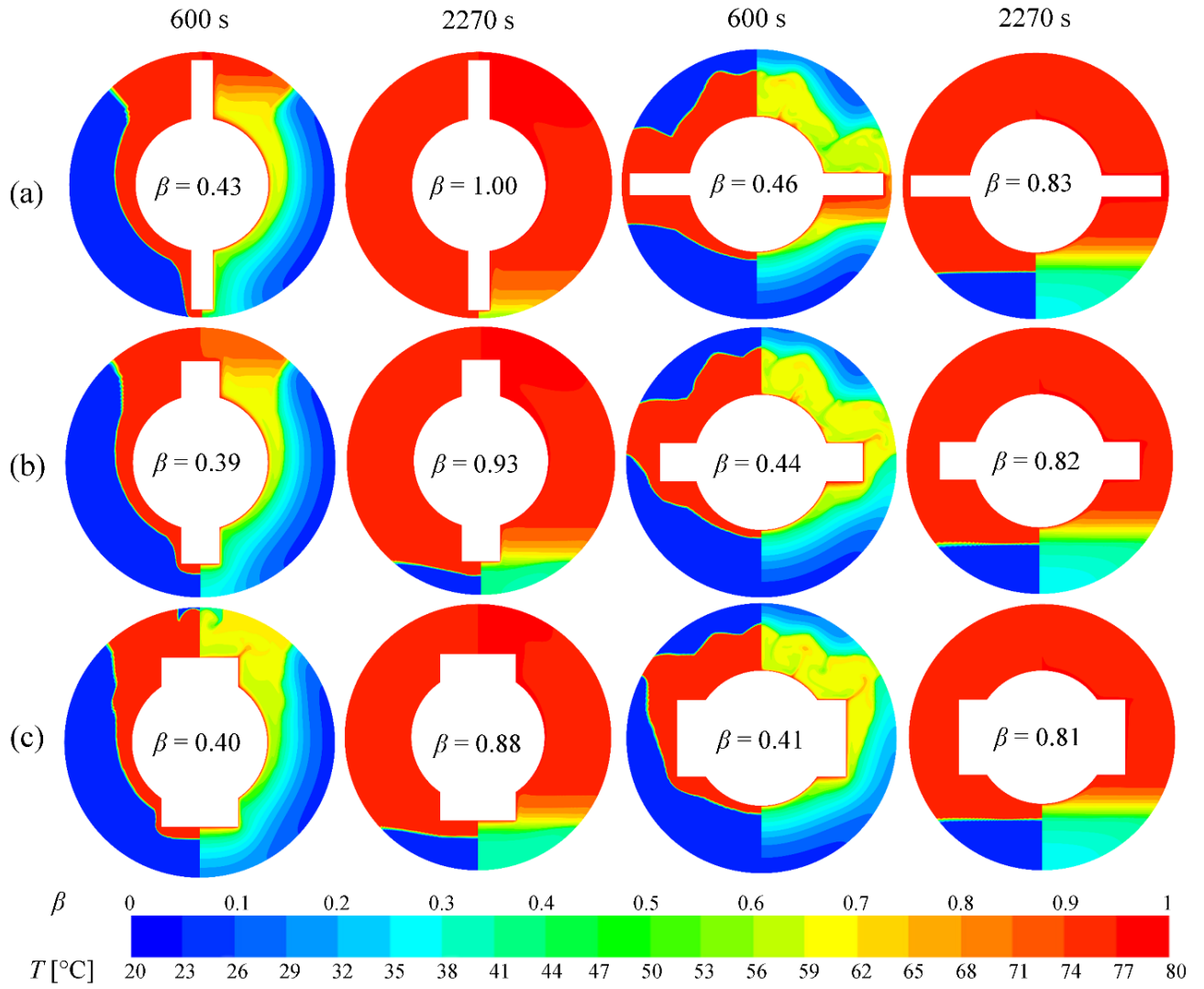
580

Figure 8 – Solid-liquid interface for different moments of the melting process for  $AR = 1/4, 1/2$  and  $7/8$  and  $\phi =$  (a) 0.003, (b) 0.005, (c) 0.01, (d) 0.02 and (e) 0.03.



581

582 Figure 9 – Liquid fraction ( $\beta$ ) vs.  $Fo$ , for vertical and horizontal fins, with  $AR = 7/8$ ,583  $3/4, 1/2, 1/4$ , and  $1/8$  for  $\phi$ : (a) 0.003, (b) 0.005, (c) 0.01, (d) 0.02, and (e) 0.03.

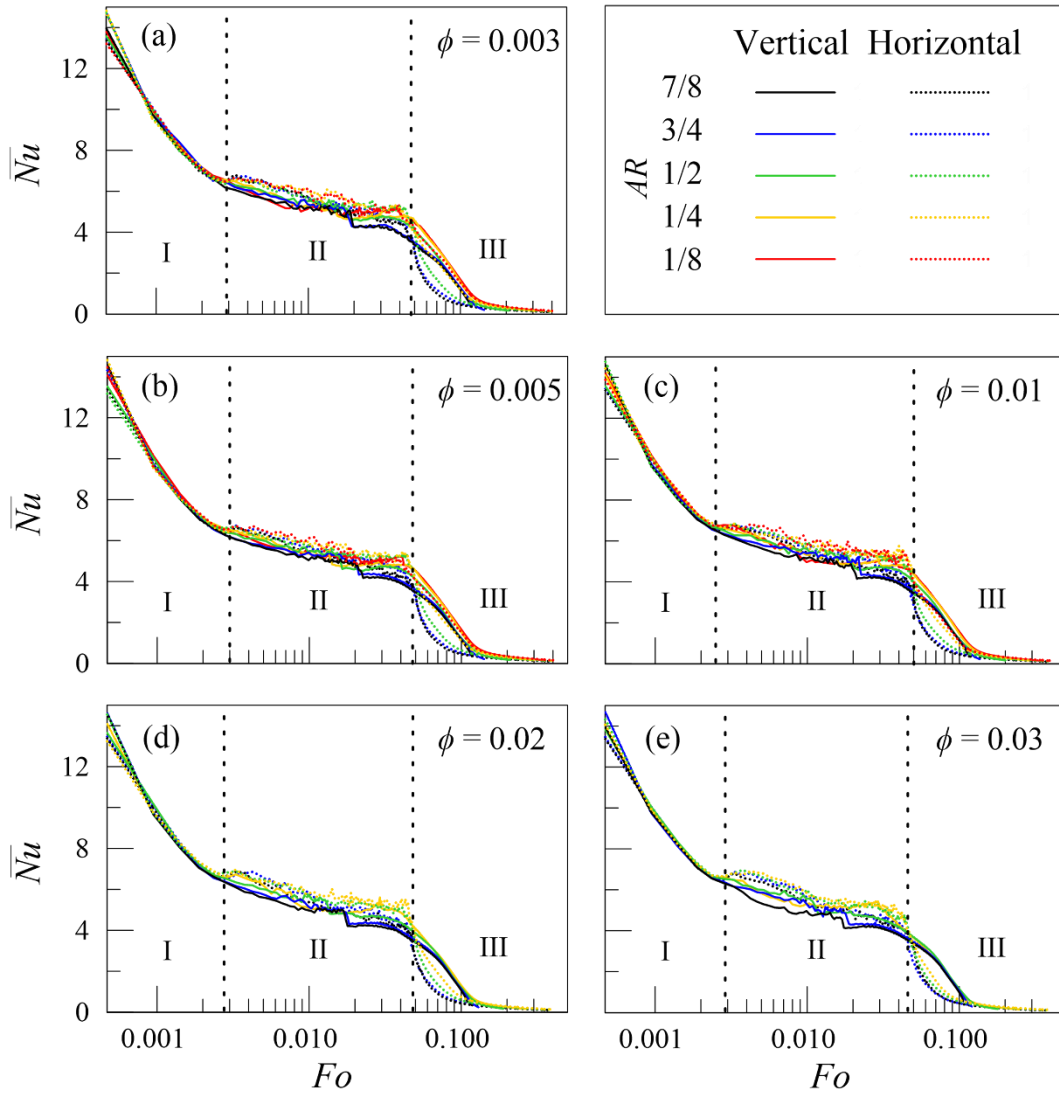


584

585

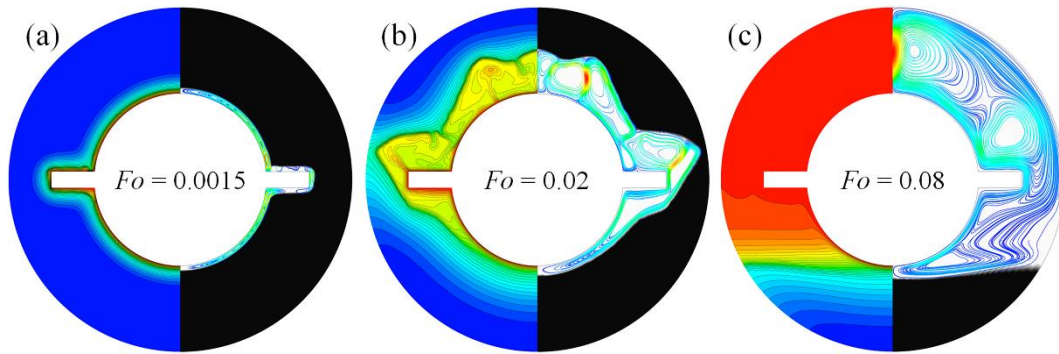
586

Figure 10 – Fields of  $\beta$  (left) and  $T$  (right), at  $t = 600$  and  $2,270$  s, for vertical and horizontal fins, with  $\phi = 0.03$  and  $AR$ : (a)  $7/8$ , (b)  $1/2$ , and (c)  $1/4$ .



587

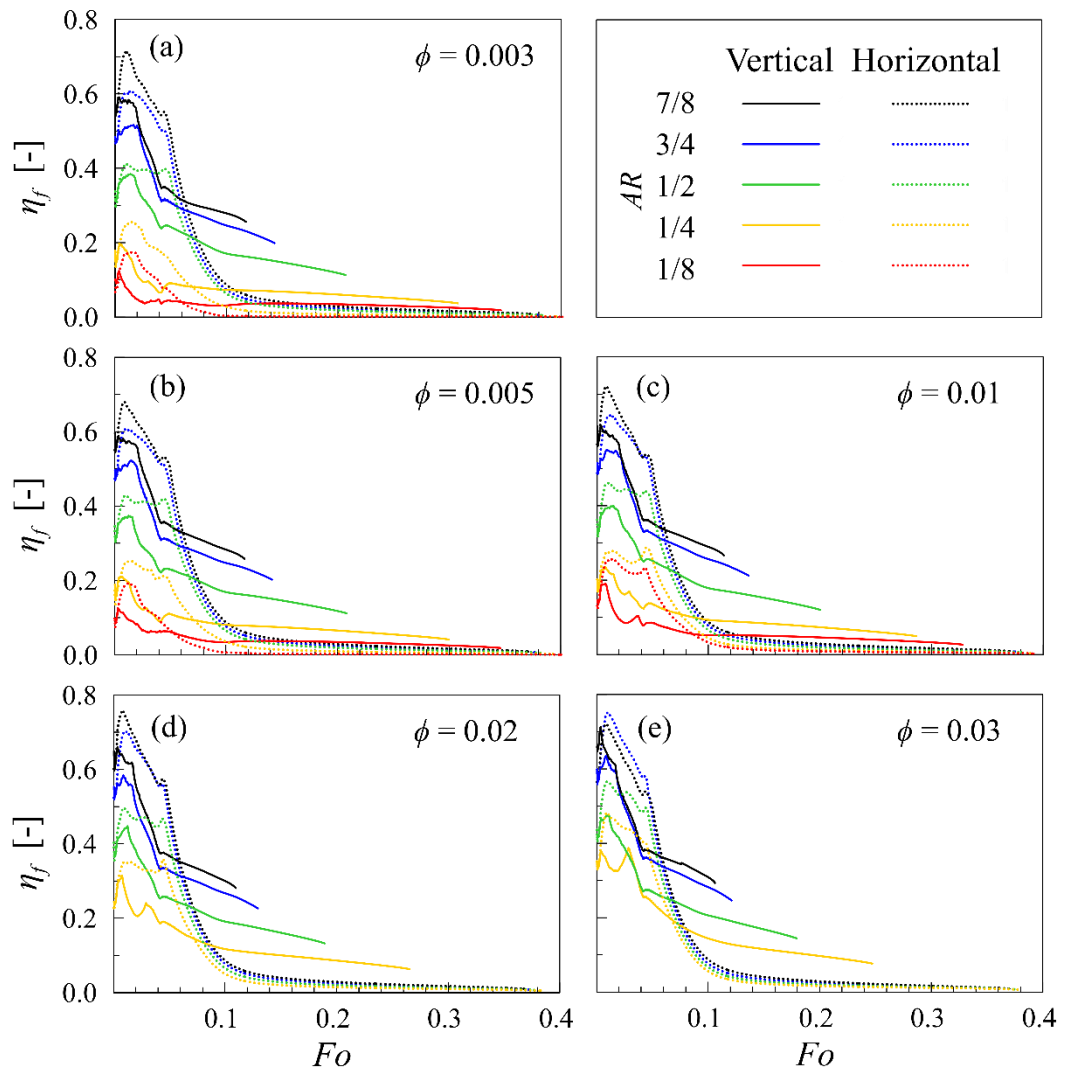
588 Figure 4 –  $\overline{Nu}$  vs.  $Fo$  for vertical and horizontal fins, with  $AR = 7/8, 3/4, 1/2, 1/4,$  and  
 589  $1/8$  for  $\phi$ : (a) 0.003, (b) 0.005, (c) 0.01, (d) 0.02, and (e) 0.03.



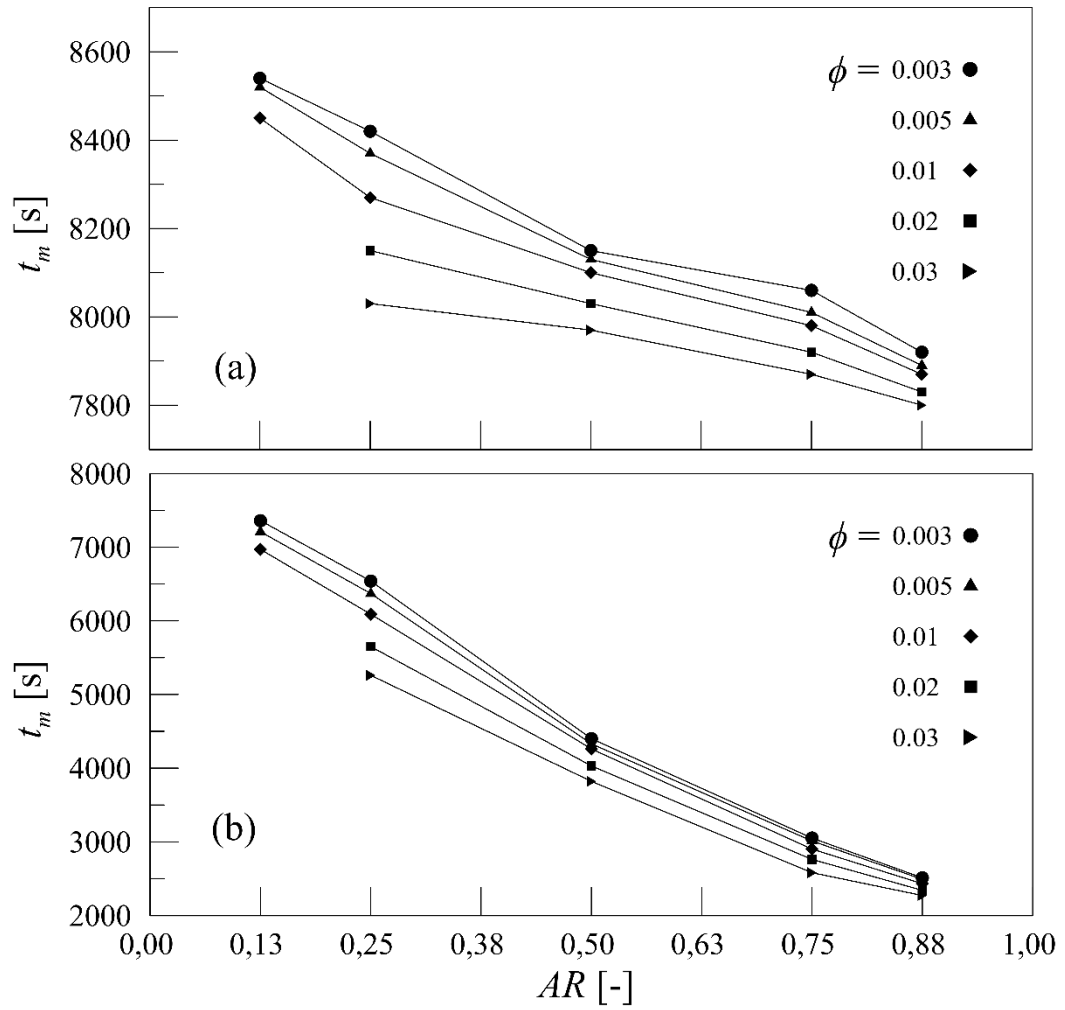
590

591 Figure 12 - Fields of  $T$  (left) and streamlines (right), for horizontal fins, with  $\phi = 0.01$ ,  
592 and  $AR = 1/2$ , at  $Fo$ : (a) 0.0015, (b) 0.02, and (c) 0.08.

593

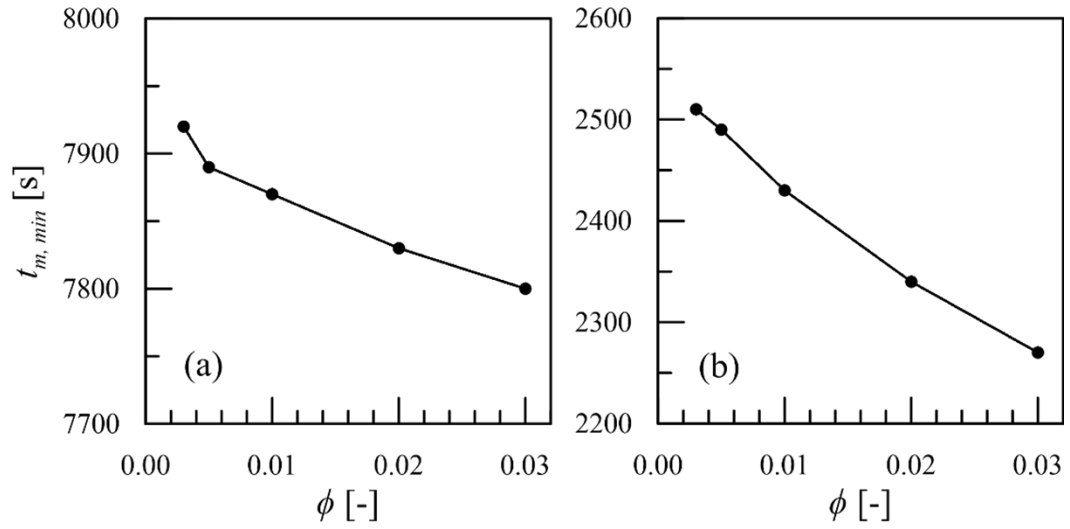


594 Figure 5 – Melting rate effectiveness ( $\eta_f$ ) vs.  $Fo$ , for vertical and horizontal fins, with  
 595  $AR = 7/8, 3/4, 1/2, 1/4,$  and  $1/8$  for  $\phi$ : (a) 0.003, (b) 0.005, (c) 0.01, (d) 0.02, and  
 596 (e) 0.03.



597  
598

Figure 6 – Total melting time ( $t_m$ ) vs.  $AR$  for  $\phi = 0.003, 0.005, 0.01, 0.02,$  and  $0.03$ :  
(a) horizontal fins and (b) vertical fins.



599 Figure 7 – Minimum total melting time ( $t_{m, min}$ ) vs.  $\phi$  for: (a) horizontal fins and  
600 (b) vertical fins, both for  $AR = 0.88$  (7/8).

601  
602

Table 1 – Fin dimensions.

		AR					
		1/8	1/4	1/2	3/4	7/8	
$\phi$	0.003	$e_f$	4.00	2.00	1.00	0.67	0.57
		$l_f$	2.50	5.00	10.00	15.00	17.50
	0.005	$e_f$	7.54	3.77	1.88	1.26	1.08
		$l_f$	2.50	5.00	10.00	15.00	17.50
	0.01	$e_f$	15.08	7.54	3.77	2.51	2.15
		$l_f$	2.50	5.00	10.00	15.00	17.50
	0.02	$e_f$	30.16	15.08	7.54	5.03	4.31
		$l_f$	2.50	5.00	10.00	15.00	17.50
	0.03	$e_f$	45.24	22.62	11.31	7.54	6.46
		$l_f$	2.50	5.00	10.00	15.00	17.50

603

Table 2 – Thermophysical properties of lauric acid (Yuan et al. [23])

$T_m$	$c_p$	$k$	$Z$	$L$	$\rho$	$\mu$		
[°C]	[J kg <sup>-1</sup> K <sup>-1</sup> ]	[W m <sup>-1</sup> K <sup>-1</sup> ]	[K <sup>-1</sup> ]	[J kg <sup>-1</sup> ]	[kg/m <sup>3</sup> ]	[kg m <sup>-1</sup> s <sup>-1</sup> ]		
					60 °C	60 °C	70 °C	80 °C
44.2	2300	0.147	0.000615	173800	863	0.00534	0.00427	0.00347